OXFORD

Human Molecular Genetics, 2016, Vol. 25, No. 10 1900–1911

doi: 10.1093/hmg/ddw063
Advance Access Publication Date: 23 February 2016
Original Article

ORIGINAL ARTICLE

Defective membrane fusion and repair in *Anoctamin5*-deficient muscular dystrophy

Danielle A. Griffin[1], Ryan W. Johnson[1], Jarred M. Whitlock[7], Eric R. Pozsgai[1,6], Kristin N. Heller[1], William E. Grose[1], W. David Arnold[3,4,5], Zarife Sahenk[1,2,3], H. Criss Hartzell[7] and Louise R. Rodino-Klapac[1,2,6,*]

[1]Center for Gene Therapy, The Research Institute at Nationwide Children's Hospital, [2]Department of Pediatrics, [3]Department of Neurology, [4]Department of Physical Medicine and Rehabilitation, [5]Department of Neuroscience and [6]Integrated Biomedical Science Graduate Program, College of Medicine, The Ohio State University, Columbus, OH, USA and [7]Department of Cell Biology, Emory University School of Medicine, Atlanta, GA, USA

*To whom correspondence should be addressed at: Center for Gene Therapy, The Research Institute at Nationwide Children's Hospital, Room 3016, 700 Children's Dr., Columbus, OH 43205, USA. Email: louise.rodino-klapac@nationwidechildrens.org

Abstract

Limb-girdle muscular dystrophies are a genetically diverse group of diseases characterized by chronic muscle wasting and weakness. Recessive mutations in *ANO5 (TMEM16E)* have been directly linked to several clinical phenotypes including limb-girdle muscular dystrophy type 2L and Miyoshi myopathy type 3, although the pathogenic mechanism has remained elusive. *ANO5* is a member of the Anoctamin/TMEM16 superfamily that encodes both ion channels and regulators of membrane phospholipid scrambling. The phenotypic overlap of *ANO5* myopathies with dysferlin-associated muscular dystrophies has inspired the hypothesis that *ANO5*, like dysferlin, may be involved in the repair of muscle membranes following injury. Here we show that *Ano5*-deficient mice have reduced capacity to repair the sarcolemma following laser-induced damage, exhibit delayed regeneration after cardiotoxin injury and suffer from defective myoblast fusion necessary for the proper repair and regeneration of multinucleated myotubes. Together, these data suggest that ANO5 plays an important role in sarcolemmal membrane dynamics. Genbank Mouse Genome Informatics accession no. 3576659.

Introduction

The importance of muscle mass and strength for daily activities such as locomotion and breathing and for whole body metabolism is unequivocal. Deficits in muscle function produce muscular dystrophies (MDs) that are characterized by muscle weakness and wasting and have serious impacts on quality of life (1). The most well-characterized MDs result from mutations in genes encoding members of the *dystrophin-associated protein complex* (DAPC) (2). These MDs result from membrane fragility associated with the loss of sarcolemmal-cytoskeleton tethering by the DAPC (3,4). In contrast, a subset of other MDs is thought to be caused by defects in sarcolemmal repair. Due to the mechanical stress the sarcolemma experiences during contraction, even healthy muscle is in constant need of repair mechanisms to patch injured membrane (4). Sarcolemmal patch repair relies on the fusion of membrane vesicles at sites of damage (5,6), and the attenuation of this process is considered a putative cause of dysferlinopathies, MDs caused by mutations in dysferlin (7–9).

Recently, a new MD with features similar to dysferlinopathies and characterized by sarcolemmal lesions has been linked to recessive mutations in *ANO5 (TMEM16E)* (10–12). *ANO5* mutations produce limb-girdle muscular dystrophy type 2L (LGMD2L) and Miyoshi myopathy dystrophy type 3 (MMD3). The phenotype associated with *ANO5* mutations is variable, but typically the disease presents in adulthood (age 20–50) with proximal lower

Received: November 23, 2015. **Revised:** January 20, 2016. **Accepted:** February 22, 2016

limb weakness, high serum creatine kinase levels, asymmetric muscle atrophy and weakness, and is typically accompanied by sarcolemmal lesions, similar to dysferlinopathy (10–12). To date, ~72 different *ANO5* mutations have been reported in MD patients (Supplementary Material, Fig. S1), and screens for *ANO5* mutations in LGMD patients lacking mutations in other known LGMD genes indicate that *ANO5* mutations may be one of the more common causes of LGMD (10,11,13).

The ANO/TMEM16 family is functionally split into two categories. The founding members, *ANO1 (TMEM16A)* and *ANO2 (TMEM16B)* encode calcium-activated chloride channels (14–16), while other ANOs fail to conduct chloride and have roles in phospholipid scrambling (PLS) (17–20). However, ANO5 has not been found to exhibit either of these two activities at the plasma membrane (21,22), suggesting a novel function in skeletal muscle. This is consistent with experimental evidence demonstrating that ANO5 is enriched in internal membranes in muscle fibers (23). Given this novelty, it remains unclear how deficiency in ANO5 function elicits a LGMD phenotype, and specifically why *ANO5* mutations manifest in a clinically similar way to dysferlin-associated MD.

Here we report the creation of an *Ano5* knockout mouse model that recapitulates features of human LGMD2L patients. We show that disruption of the *Ano5* gene in mice produces several dystrophic histopathologic features, exercise intolerance, dysfunction in sarcolemmal repair and myoblast fusion defects. We hypothesize that these defects are related to changes in subcellular membrane and/or sarcolemmal membrane dynamics mediated by ANO5.

Results

Generation of an Ano5$^{-/-}$ mouse model

To generate an *Ano5* knockout model, we used a vector targeting *Ano5* from exon 8 to exon 9 to produce a truncated transcript (Fig. 1A). The targeting construct was designed as a 'knockout first' (24) so that a null allele is generated through splicing to a *lacZ* trapping element. The targeting cassette was inserted following exon 8 with flanking *FRT* and *loxP* sites present to generate a conditional allele if embryonic lethality was noted (24,25) (Fig. 1A). Following embryonic stem cell targeting and transfer, the genotypes were verified by genomic PCR (Fig. 1B). RT–PCR using primers spanning exons 10–14 (e10–e14) or exons 17–20 (e17–e20) shows a loss of transcript distal to the *lacZ* insertion cassette (Fig. 1C). Consistent with these data, quantitative RT–PCR demonstrates ~80% reduction in pre-cassette *Ano5* transcript and >99% reduction of post-cassette *Ano5* transcript in all muscles tested (Fig. 1D). To determine whether Ano5 protein expression was reduced, muscle lysates were run on SDS–PAGE gels and western blots prepared. The presence of major muscle protein migrating at the same molecular weight as Ano5 (~107 kDa) precluded a clean western blot and thus extracts were run under non-denaturing conditions on a native blue gel. Under these conditions, Ano5 migrates as a broad band ~420 kDa in addition to two bands of larger mass. These bands represent either oligomers of Ano5 or complexes of Ano5 with its binding partners. Similar results have been recently reported by Gyobu *et al.* (26). Regardless, no protein signal is observed in *Ano5*$^{-/-}$ muscle. Surprisingly, a greatly reduced signal is also observed in the heterozygote (Fig. 1E). No overt histological phenotypes were seen in *Ano5*$^{+/-}$ mice, consistent with the recessive nature of MDs due to *ANO5* mutations. No embryonic lethality was noted in *Ano5*$^{-/-}$ animals. As *Ano5* shares a significant sequence homology to *Ano6*, and Ano6 is known to be expressed in skeletal muscle under some conditions (27), RT–PCR was performed to measure relative expression of *Ano6* cDNA of *Ano5*$^{-/-}$ mouse muscles. Quantitative RT–PCR demonstrates a modest, but statistically insignificant elevation of *Ano6* transcript in *Ano5* deficient muscles (Supplementary Material, Fig. S2).

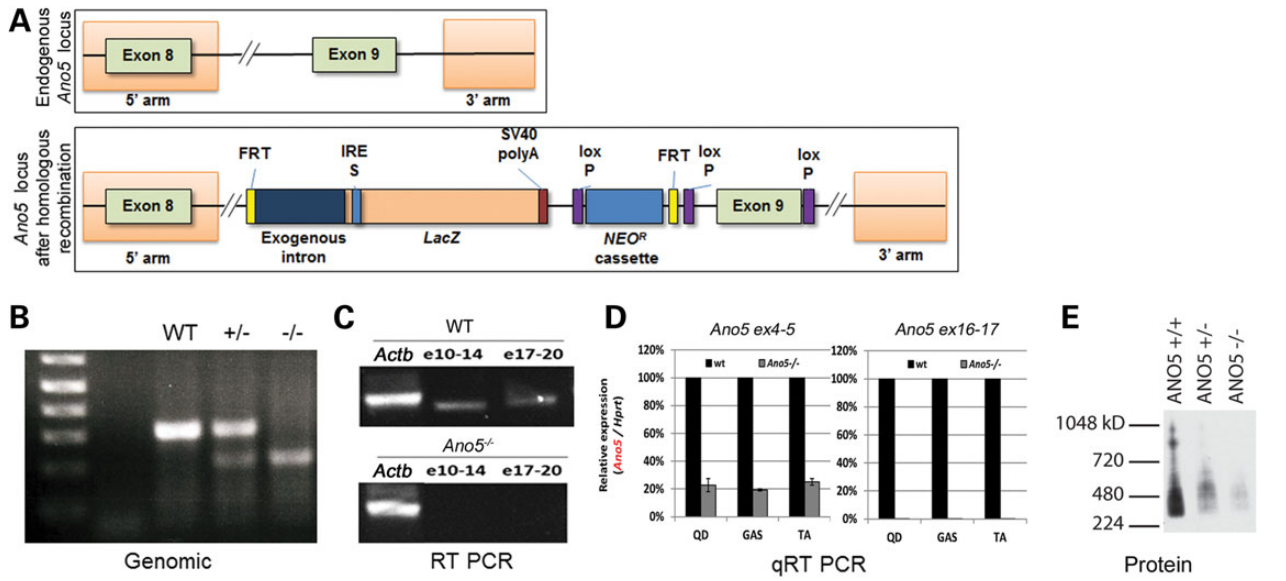

Figure 1. Generation of the *Ano5*$^{-/-}$ mouse model. (**A**) An *Ano5* targeting vector was used to include an exogenous intron and *lacZ*-encoding exon with a polyadenylation termination signal. The resulting mRNA terminates with exon 8. (**B**) Genomic DNA isolated from tail clippings of littermates. (Lane 1) WT mouse, (Lane 2) *Ano5*$^{+/-}$, (Lane 3) *Ano5*$^{-/-}$; WT allele: 300 bp fragment, *Ano5* allele: 200 bp fragment. (**C**) RT–PCR displaying reduced *Ano5* transcript in *Ano5*$^{-/-}$ muscle tissue using two primer sets targeting *Ano5*. Lane 1: *β-actin* control; lane 2 (e10–e14), primers spanning exons 10–14; lane 3 (e17–e20) primers spanning exons 17–20. (**D**) Approximately 80% and >99% relative reduction of *Ano5* transcript, at the 5′ and 3′ end, respectively, was confirmed through qRT–PCR in quadriceps (QD), gastrocnemius (GAS) and tibialis anterior (TA) muscle extracted from the *Ano5*$^{-/-}$ mouse ($P < 0.001$). (**E**) Ano5 protein expression is absent in *Ano5*$^{-/-}$ mice. Western blot of blue native gel of muscle extracts from WT, *Ano5*$^{+/-}$ and *Ano5*$^{-/-}$ mice. WT Ano5 runs as a broad smear that centers around 400 kDa. The broad band may be explained by protein glycosylation, ubiquitination and/or multimerization. Ano5 is present, although greatly reduced in the heterozygote and is barely detectable in the knockout.

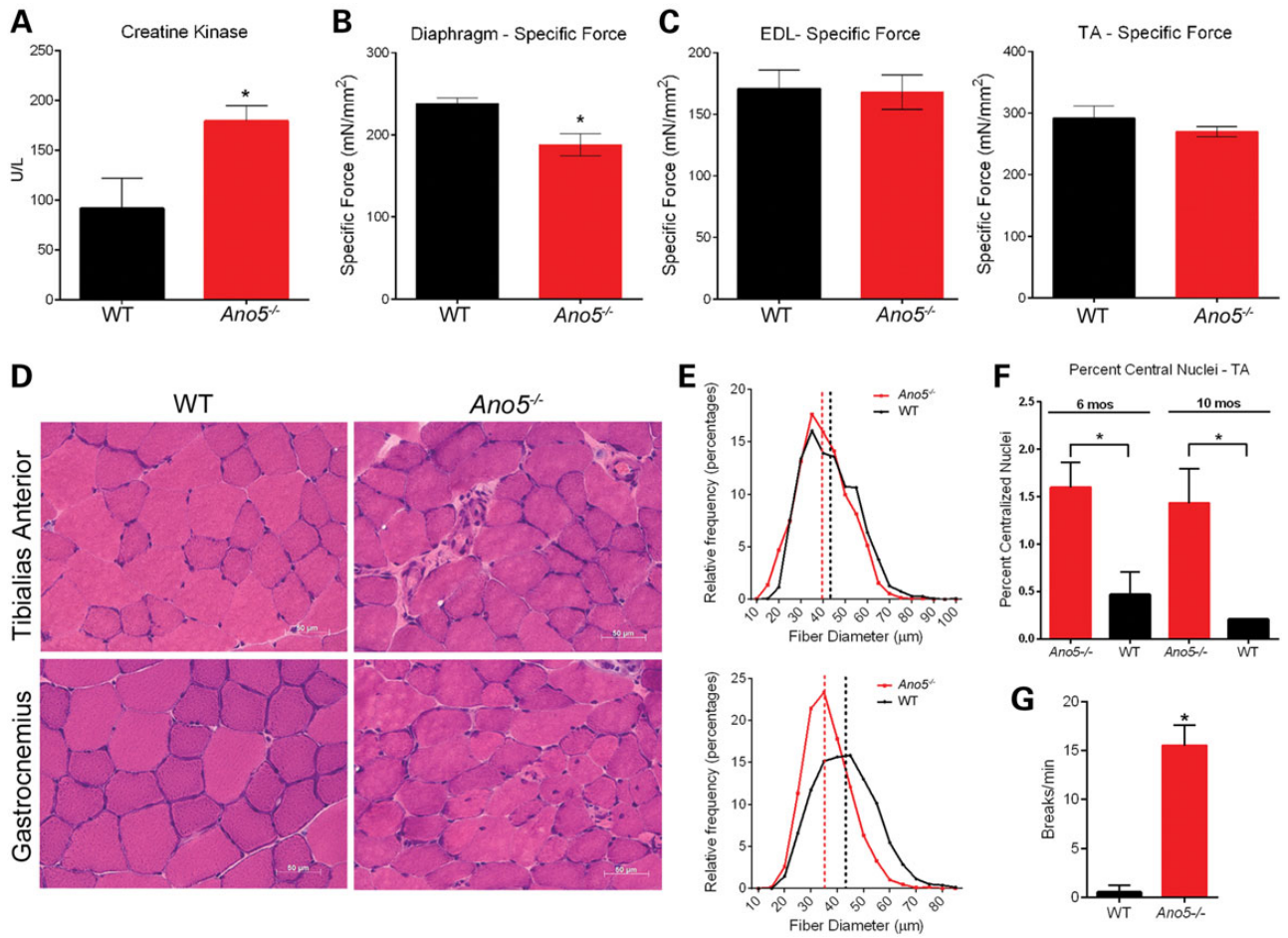

Figure 2. Characterization of *Ano5*$^{-/-}$ deficient mice. (**A**) Serum creatine kinase is significantly elevated in *Ano5*$^{-/-}$ mice 179.3 ± 15.52, $n = 5$ at 9 months compared with aged-matched controls 91.73 ± 30.13, $n = 4$ ($P < 0.05$). (**B**) Specific force of contraction of diaphragm strips from 10 months *Ano5*$^{-/-}$ mice 188.3 ± 13.52 was significantly decreased compared with controls 238.1 ± 6.770 ($P < 0.01$). (**C**) Specific force of contraction of EDL (9 months) and TA (4 months) muscles from *Ano5*$^{-/-}$ mice 168.0 ± 14.07 and 269.9 ± 8.54, respectively, were not significantly different than controls 170.5 ± 15.36 and 292.1 ± 19.59 ($P > 0.05$). (**D**) H&E-stained tissue sections demonstrating mild dystrophic pathology including central nuclei, fiber size variability and areas of necrosis in the TA and GAS of the *Ano5*$^{-/-}$ mouse compared with WT controls. Scale bar = 50 µm. (**E**) Muscle fiber diameter measurements showed a reduction in *Ano5*$^{-/-}$ fiber diameter compared with WT especially in GAS muscle ($P < 0.0001$). (**F**) The number of centralized nuclei are modestly increased in *Ano5*$^{-/-}$ *muscle* ($P < 0.05$) but remain stable over time comparing 6- and 10-month timepoints. (**G**) *Ano5*$^{-/-}$ mice demonstrated frequent pauses when treadmill exhaustion studies. Error bars = Mean ± SEM.

Clinical and histopathological evaluation of the Ano5$^{-/-}$ mouse

The *Ano5*$^{-/-}$ mouse exhibits many features characteristic of human *ANO5*-myopathy including increased serum creatine kinase levels, variable weakness among muscles, altered muscle fiber diameter and exercise intolerance (11,21). Serum creatine kinase is elevated ~2-fold in *Ano5*$^{-/-}$ mice (Fig. 2A). The specific force of muscle contraction is significantly decreased ~15% in diaphragm (Fig. 2B), but is essentially unaffected in extensor digitorum longus (EDL) and tibialis anterior (TA) muscles (Fig. 2C). This variability among muscles is characteristic of *ANO5* myopathies and is also observed in histological analysis of different muscles. Relative to wild-type (WT), average muscle fiber diameter is significantly smaller in gastrocnemius (GAS) muscle from *Ano5*$^{-/-}$ mice (Ano5$^{-/-}$: 35.8 ± 8.3 µm, WT: 41.8 ± 11.0 µm, $P < 0.0001$), and to a lesser extent in the TA muscle (Ano5$^{-/-}$: 38.1 ± 11.8 µm, WT: 44.3 ± 12.2 µm, $P < 0.0001$) (Fig. 2D and E). *Ano5*$^{-/-}$ muscles exhibited mild histopathology including central nuclei and occasional necrotic fibers (Fig. 2D and F). The appearance of most mouse *Ano5*$^{-/-}$ phenotypes were typically seen at 6 months of age or later (Supplementary Material, Fig. S3). This is consistent with adult-onset of LGMD2L in humans.

To evaluate exercise tolerance, aged-matched *Ano5*$^{-/-}$ and WT mice were subjected to exercise regimes weekly for 1 h for 2 months. While WT control mice ran at a consistent speed, *Ano5*$^{-/-}$ mice were prone to frequent breaks on the treadmill (14 breaks/min) where they ceased running until the treadmill belt returned to the shock plate (Supplementary Material, SV1) (Fig. 2G). Needle electromyography, evoked compound muscle action potential (CMAP) recordings and electrical impedance myography (EIM) were performed in the hindlimbs of *Ano5*$^{-/-}$ and WT mice but showed no significant changes, similar to the human disease (Supplementary Material, Fig. S3).

Another characteristic feature of human *ANO5* myopathy is the presence of an excessive number of muscle fibers with intramuscular deposits (28,29). In the *Ano5*$^{-/-}$ mouse muscle, these structures appear as sharply defined, irregularly contoured areas that stain red with a modified trichrome stain (30). Cytoplasmic aggregates were apparent beginning at 10 months of age (Fig. 3A). Because aggregates of similar appearance have been noted in normal aged mice (30,31), aggregate occurrence

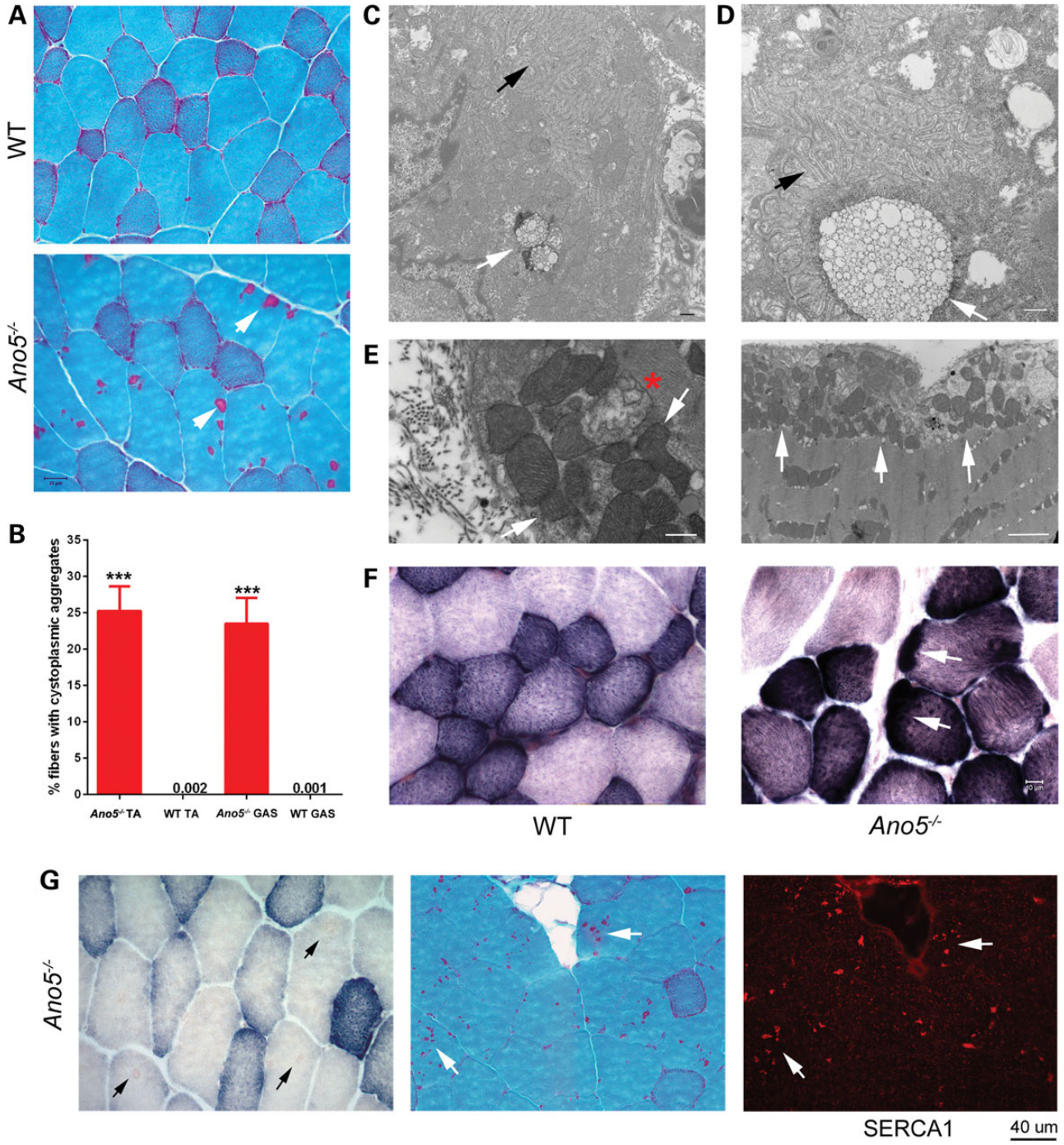

Figure 3. Subcellular histopathology in *Ano5*$^{-/-}$ muscle. (**A**) Gomori Trichrome stain of 10 months *Ano5*$^{-/-}$ and WT TA muscles. *Ano5*$^{-/-}$ muscle contains membrane aggregates (arrows). Scale bar = 20 µm. (**B**) Quantification of the number of fibers containing aggregates in TA and GAS muscles of the *Ano5*$^{-/-}$ compared with WT ($P < 0.0001$, one-way ANOVA). (**C** and **D**) Electron microscopic images demonstrating the presence of membrane aggregates in *Ano5*$^{-/-}$ muscle. Aggregates were either loosely packed, interconnecting tubular formations with fuzzy inner tubules (white arrows) or densely packed accumulations of vesicular or tubular membranes (black arrows). Scale bars = 500 nm. (**E**) Sub-sarcolemmal accumulations of mitochondria (arrows) and degenerating mitochondria (asterisk) were frequently identified by electron microscopy in *Ano5*$^{-/-}$ muscle. Scale bars = 500 nm (left) and 2 µm (right). (**F**) Succinate dehydrogenase staining of 10 months *Ano5*$^{-/-}$ TA muscle showed sarcolemmal thickening and capped fibers that were not present in WT. Scale bars = 10 µm. (**G**) Cryosections of the TA muscle from 10 months *Ano5*$^{-/-}$ mice were stained for succinate dehydrogenase (SDH). Arrows indicate reddish aggregates that do not stain for SDH (left). Serial sections from 10 months *Ano5*$^{-/-}$ mice demonstrate that many membrane aggregates (white arrows) observed with trichrome staining are positive for SERCA1 (right) suggesting they are derived from the sarcoplasmic reticulum. Scale bar = 40 µm.

was quantified. Approximately 25% of *Ano5*$^{-/-}$ fibers displayed irregularly contoured red areas upon trichrome staining, while <0.02% of age-matched control fibers had these aggregates (Fig. 3B). Electron microscopy (EM) revealed that the aggregates comprised membranous material. Many *Ano5*$^{-/-}$ muscle fibers exhibited densely packed accumulations of vesicular or tubular

membranes or haphazardly oriented and loosely packed interconnecting tubular formations with fuzzy inner tubules that corresponded to the aggregates seen in light microscopy (Fig. 3C and D). *Ano5*$^{-/-}$ mice showed similar pathology findings consistent with that of *ANO5* patients. EM of patient muscle compound heterozygous for two mutations [c.155A > G (p.Asn52Ser)] + [c.191dupA (p.Asn64Lysfs*15)] in the coding region of the *ANO5* gene revealed numerous aggregates and multiple sites displaying areas of degenerating mitochondria (Supplementary Material, Fig. S4). Aggregates in *Ano5*$^{-/-}$ muscle stained positive for SERCA1 but not succinate dehydrogenase (SDH) activity, suggesting that they are derived from the sarcoplasmic reticulum and not from mitochondria (Fig. 3G) (30,31). However, *Ano5*$^{-/-}$ mice did exhibit degenerating mitochondria and sub-sarcolemmal mitochondrial accumulation in addition to these membrane aggregates (Fig. 3E). The sub-sarcolemmal accumulation of mitochondria was confirmed by staining frozen sections for SDH, which was localized in dense patches near the surface of muscle fibers (Fig. 3F). To identify whether the mitochondrial degeneration observed had functional significance, we quantified citrate synthase activity as a measure of intact mitochondria and found there was a significant decrease in *Ano5*$^{-/-}$ muscle extracts compared with WT controls (Supplementary Material, Fig. S5).

Ano5 facilitates membrane repair

In healthy individuals, normal exercise results in small lesions in the plasma membrane that are healed by two processes: (i) small tears are resealed by assembly of new plasma membrane and (ii) sites of more severe disruption are repaired by satellite cells that proliferate and differentiate into myocytes that fuse to repair or regenerate multinucleated muscle fibers (32). To test the effect of loss of *Ano5* expression on membrane repair, we first examined the effect of membrane damage produced by an intense laser pulse delivered to isolated flexor digitorum brevis (FDB) muscle fibers of 4-month-old mice (Fig. 4A and B). Membrane damage was assessed by accumulation of FM1-43, a membrane-impermeant styryl cationic dye that is not fluorescent in aqueous solution but fluoresces brightly in a lipid environment and has been used extensively to study membrane repair (9,33,34). A small area of fluorescence was detected at the site of damage in WT and *Ano5*$^{-/-}$ fibers immediately after laser injury (Fig. 4A). The

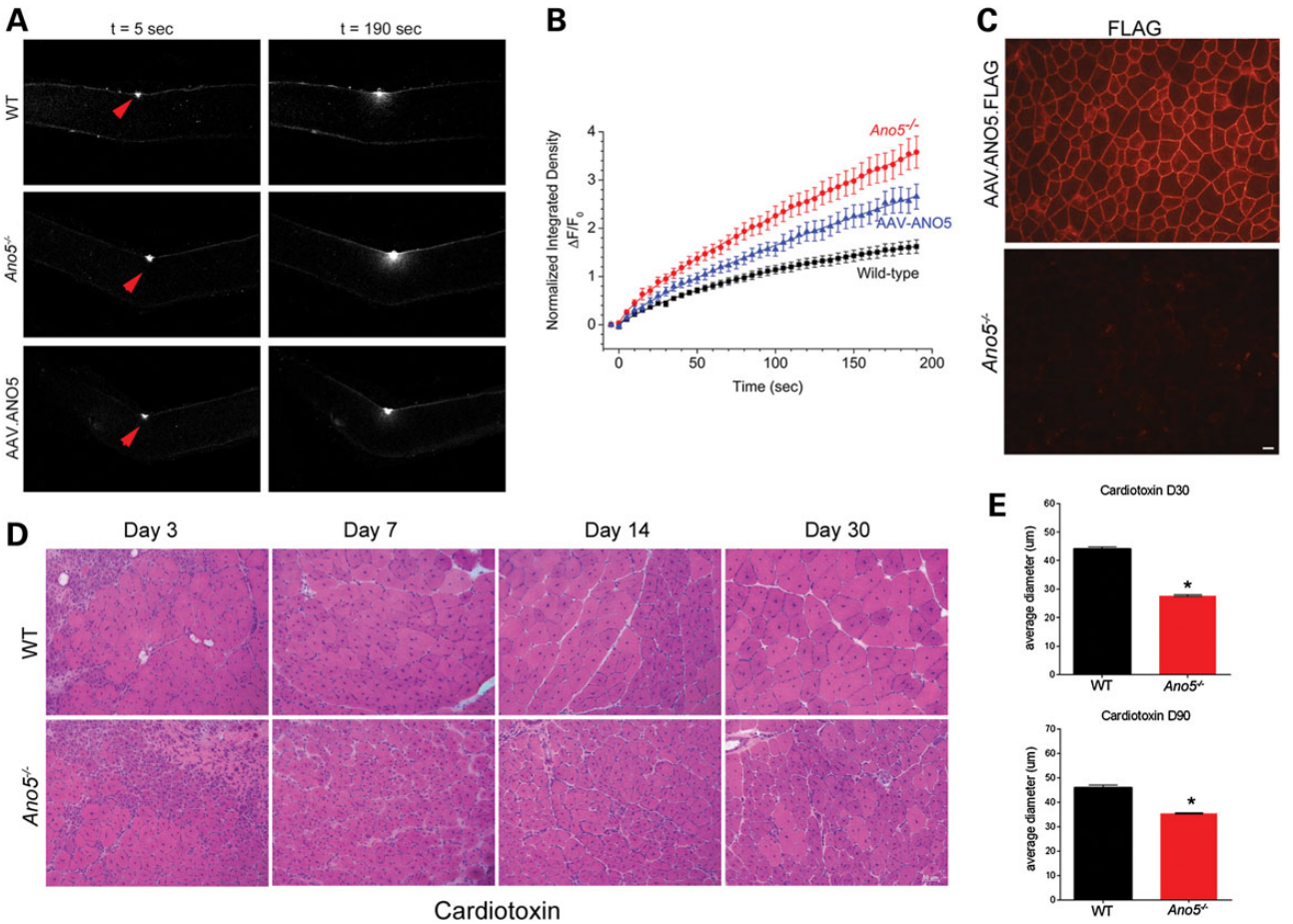

Figure 4. Membrane Repair is defective in *Ano5*$^{-/-}$ mice. (**A**) Images of *Ano5*$^{-/-}$ and WT muscle 4-month-old mice damaged by a laser pulse shown 5 and 190 s post-injury. Red arrows indicate the site of damage with FM1-43 dye accumulating quickly in *Ano5*$^{-/-}$ muscle compared with WT and *Ano5*$^{-/-}$ following delivery of 1×10^{11} vg AAV. ANO5.FLAG vector. Scale bar = 50 μm. (**B**) Measurement of fluorescence intensity after laser-induced injury. *Ano5*$^{-/-}$ muscle is statistically different from WT and AAV. ANO5 fibers at all times >100 s post-injury (two-way ANOVA, $P < 0.001$). (**C**) Expression of ANO5-FLAG in *Ano5*$^{-/-}$ uninjected TA or TA injected with 5×10^{10} vg AAV. ANO5.FLAG vector. Immunofluorescence with anti-FLAG antibody demonstrated ANO5-FLAG expression following intramuscular injection (top) that was absent in untreated *Ano5*$^{-/-}$ muscle (bottom). Scale bar = 40 μm. (**D**) Recovery from cardiotoxin-induced muscle damage. H&E-stained tissue sections of WT and *Ano5*$^{-/-}$ TA muscles at 1, 3, 7, 14, 30 and 90 days post-cardiotoxin injection (Days 3,7,14 and 30 shown). *Ano5*$^{-/-}$ muscle incurred more damage and showed impairment in regeneration compared with WT. (**E**) Myofiber size remains statistically smaller in *Ano5*$^{-/-}$ muscle at 30 and 90 days compared with WT at 30 days (Cardiotoxin D30) and 90 days (Cardiotoxin D90) post-cardiotoxin injection ($P < 0.05$).

increase in fluorescence was greater and occurred at a ~2-fold faster initial rate in *Ano5*$^{-/-}$ muscle fibers than in WT fibers. Whereas the fluorescence appeared to be leveling off at 190 s in WT, the fluorescence continued to increase in Ano5$^{-/-}$ fibers for the duration of the experiment (Fig. 4B). To test whether the defect in membrane repair was directly related to *Ano5* expression, we expressed human *ANO5* cDNA using adeno-associated virus (AAV) in the *Ano5*$^{-/-}$ muscles. AAV.ANO5 partially restored membrane resealing in *Ano5*$^{-/-}$ muscle (Fig. 4B). Intramuscular delivery of AAV.ANO5.FLAG results in sarcolemmal ANO5 expression in *Ano5*$^{-/-}$ mice (Fig. 4C).

Impaired regeneration in Ano5 KO mice

We then asked whether muscle regeneration was also defective in *Ano5*$^{-/-}$ mice. This was done by examining the ability of the muscle to recover from injury produced by cardiotoxin injection (35) (Fig. 4D). To track temporal changes of necrosis and regeneration, TA and GAS muscles of 8-week-old mice were injected with cardiotoxin three times, spaced 2 weeks apart. Tissues were harvested 1, 3, 7, 14, 30 and 90 days after the final injection (Fig. 4D). The contralateral side was used as a saline-only control. The WT muscle regenerated after cardiotoxin treatment, so that by 1 month the muscle appeared largely normal with the exception of central nuclei in newly regenerated fibers. However, in *Ano5*$^{-/-}$ mice, there was an extensive delay in regeneration and longstanding necrosis. After 3 months, the mean fiber diameter of *Ano5*$^{-/-}$ muscle remained significantly reduced compared with WT and many fibers exhibited central nuclei (Fig. 4D and E).

Loss of Ano5 leads to a myoblast fusion defect

Because cardiotoxin damages only muscle fibers but not satellite cells (35), the slow recovery of *Ano5*$^{-/-}$ muscle after cardiotoxin injection suggests that muscle regeneration is defective in *Ano5*$^{-/-}$ mice. In addition to a membrane patching mechanism to repair damaged sarcolemma, adult muscle requires muscle progenitor satellite cells that proliferate, differentiate and fuse to repair/replace damaged muscle fibers *in vivo* (32). Many LGMD2L patients first manifest clinical symptoms after a significant muscle injury that persists longer than normal (29). This led us to hypothesize that the progenitor cell population in these individuals may have a decreased ability to repair damaged muscle fibers in addition to the sarcolemmal patch repair defect we characterized in Figure 4. To test this, we isolated this myoblast progenitor population from 3-month-old *Ano5*$^{-/-}$ mice and compared the fusogenic properties of these cells with age-matched WT controls from the same genetic background.

First, we assessed the ability of the myoblast progenitor cell populations from *Ano5*$^{-/-}$ mice to fuse compared with WT cells. To quantify myoblast fusion, we stained cells with a marker of differentiated muscle (myosin heavy chain, MHC) and a nuclear stain to count the number of nuclei that had incorporated into multinucleated myofibers. As shown in Figure 5A–C, after 3 days 73% of wild-type cells had fused to form multinucleated MHC-positive myotubes, while only 48% of *Ano5*$^{-/-}$ cells had fused. Furthermore, we observed that the *Ano5*$^{-/-}$ myotubes were generally shorter and a large fraction exhibited an ovoid shape instead of the elongated shape seen in WT cells (Fig. 5A and B). To quantify this fusion defect further, we counted the number of nuclei in each myotube. *Ano5*$^{-/-}$ myotubes on average had fewer nuclei than WT myotubes (Fig. 5D and E). While ~50% of WT myotubes had >6 nuclei, <10% *Ano5*$^{-/-}$ myotubes had this many nuclei. Taken together, the cardiotoxin and myoblast fusion assays demonstrate that both *Ano5*$^{-/-}$ mature myocytes and myoblast progenitors are fusion defective. This defect likely contributes to the failed muscle regeneration and resultant progressive muscle wasting indicative of LGMD2L and MMD3.

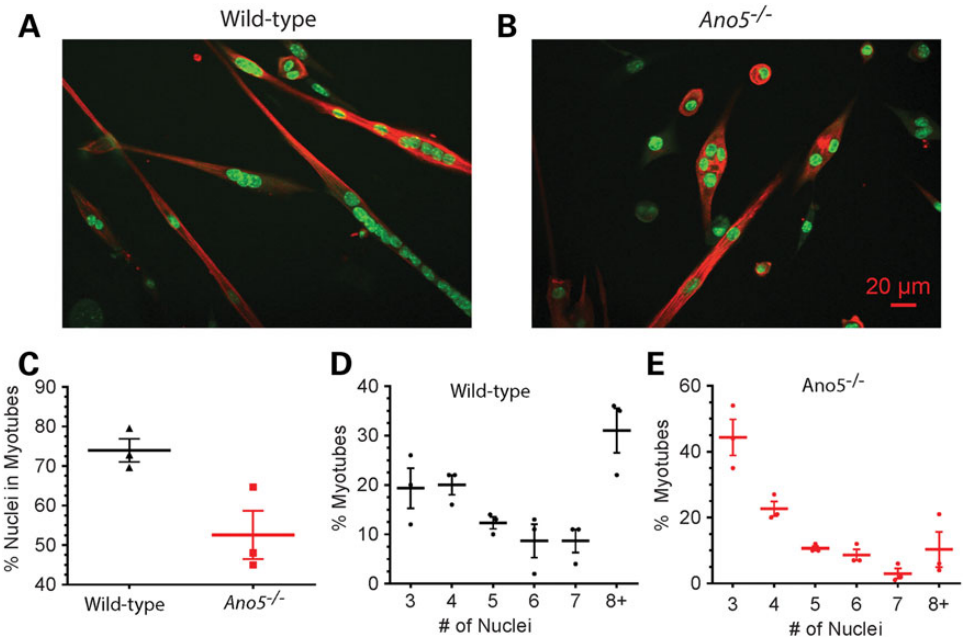

Figure 5. Loss of *Ano5* expression impairs myoblast fusion. (**A** and **B**) Confocal images of primary myoblast cultures isolated from adult WT (**A**) and *Ano5*$^{-/-}$ (**B**) mice differentiated for 3 days on glass coverslips, fixed and stained for MHC with antibody (red) and nucleic acid (Syto24, green). (**C**) Fusion index (mean ± SEM). There was a significant reduction in fusion competence between WT (73%) and *Ano5*$^{-/-}$ (48%) myoblasts ($P < 0.03$) (**D** and **E**). The average number of nuclei per myotube was measured from the same three experiments for WT (**D**) and *Ano5*$^{-/-}$ (**E**). In (C–E), individual data points indicate mean values for each of three independent experiments with a total of >12 000 nuclei counted.

Discussion

Here we demonstrate an essential role for ANO5 in muscle regeneration and repair. Loss of ANO5 causes a dystrophic phenotype in mice, reminiscent of LGMD2L patients, with mild histopathology that varies among muscles, exercise intolerance, impaired regeneration and elevated creatine kinase levels. Mitochondrial abnormalities were observed in both young and aged *Ano5*$^{-/-}$ mice. In addition to the structural defects the mitochondria displayed through electron microscopic imaging, we also demonstrated functional loss using quantitative enzyme analysis of citrate synthase indicating the presence of damaged mitochondria. The structural and functional mitochondrial findings may provide some clarification behind the underlying and unexplained symptoms of exercise intolerance and myalgia reported by *ANO5*$^{-/-}$ patients (36) and replicated in *Ano5*$^{-/-}$ mice. We also characterize an attenuation of sarcolemmal patch repair in *Ano5*$^{-/-}$ fibers that is partially rescued by viral expression of human ANO5 and find that the disruption of *Ano5* perturbs the fusogenic quality of primary myoblasts as well as mature myocytes. The mitochondrial defects may be secondary to failed membrane repair and/or regeneration or rather represent a defect that is universal to all membranes including intracellular membrane-bound organelles.

Another noteworthy finding of this study was that the membrane aggregates observed in *Ano5*$^{-/-}$ knockout animals are very similar to tubular aggregates that have been reported in mice with STIM1 or ORAI1 genes disrupted (37,38). The mechanisms of formation of tubular aggregates remains unknown, but because STIM1 and ORAI1 are involved in store-operated Ca^{2+} signaling, it has been suggested that they are stimulated by disrupted Ca^{2+} signaling. The fact that our aggregates stain for SERCA supports the idea that they are derived from SR, and supports the hypothesis that there is a defect in membrane trafficking and organization.

Disruption of *Ano5* closely phenocopies the loss of dysferlin expression in murine models (39), and dysferlin mutations cause MDs similar to ANO5 myopathies (LGMD2B and MMD1 versus LGMD2L and MMD3). The observation that many membrane repair-associated proteins, including dysferlin via its C2 domains, bind phosphatidylserine, and that some ANOs can scramble phosphatidylserine poses the intriguing possibility that defective PLS due to ANO5 loss may explain the similar disease phenotypes. Further, the reorganization of phosphatidylserine across muscle membranes is a plausible mechanism of action with respect to the repair and regeneration defects seen in ANO5 myopathies. PtdSer is transiently expressed at sites of contact between fusing myoblasts (40,41). Further, there is functional data that phosphatidylserine regulates myoblast fusion and that the phosphatidylserine receptors BAI1 and BAI3 are implicated in myoblast fusion (42–44). Cardiotoxin, a neurotoxin known to cause necrosis, when injected into the hindlimb muscles of *Ano5*$^{-/-}$ mice showed efficiency in causing necrosis in both the deficient and wild-type mouse models. However, the muscles of *Ano5*$^{-/-}$ mice showed a delayed ability to regenerate and a decrease in size compared with wild-type muscle. The *Ano5*$^{-/-}$ mice have a delayed muscle repair response following injury. The sequence similarity of Ano5 to Ano6 suggests strongly that Ano5 is involved in PLS. Although PLS is known to be tightly linked to membrane trafficking, it remains to be seen precisely how PLS may be involved in membrane repair. The apparent localization of Ano5 in the ER argues that the function of Ano5 may be more complex than simply exposure of phosphatidylserine to the external environment. Studies to examine whether ANO5 participates in some form of PLS and/or other processes of membrane dynamics are ongoing.

Recently, two other laboratories have reported on ANO5 knockout mice (26,45). In both cases, these investigators conclude that the *Ano5* knockout mice do not exhibit any muscle phenotype. These knockout animals were produced by disruption of exon 1 (45) or exon 2 (26), while our mice were produced by a gene trap between exon 8 and 9. Although we find no transcripts corresponding to exons downstream from exon 9, we do find a small amount of transcript corresponding to exons located 5′ to the disruption. We do not know whether any protein is translated from these transcripts, but this observation raises the possibility that partial transcripts may be produced in our animals and that these may directly or indirectly have pathogenic consequences. It is notable that one of the most common ANO5 mutations (c.191dupA) occurs in exon 5 that results in a frame shift and a stop codon. Many patients have heterozygous mutations in the ANO5 gene with one of them being c.191dupA.

This *Ano5*$^{-/-}$ mouse represents an important model for the study of *ANO5*-myopathy, sarcolemmal repair and myogenic cell fusion. Our *Ano5*$^{-/-}$ model demonstrates testable therapeutic outcomes and will allow for additional studies focused on Ano5 function and disease pathophysiology. As shown in Figure 1, the *Ano5*$^{-/-}$ mice we generated may express partial transcripts. This more closely resembles that of LGMD2L patients with pathogenic mutations identified only in exon 4 or later and the most frequent mutation (founder) located at the 5′ splice site of exon 5 (36). Here we have developed proof of principle for gene replacement therapy as a treatment strategy for *ANO5* myopathy by partially rescuing the membrane repair phenotype via AAV.ANO5 treatment of *Ano5*$^{-/-}$ mice. Additionally, we believe that this model will be important for further refinement of the ANO5 mechanism of action in sarcolemmal repair and myoblast fusion which will greatly inform the mechanistic understanding of *ANO5*-myopathy, as well as inform patient treatment strategies in the future.

Materials and Methods

Ethical statement

This study has been approved by the Animal Care and Use Committee of The Research Institute at Nationwide Children's Hospital (RINCH). All animal handling was performed in accordance with the Guidelines for Animal Experiments at RINCH. All injections were performed under anesthesia. Efforts were made to eliminate pain and suffering. Animals from both genders were used for all studies unless otherwise specified.

Generation of anoctamin5-deficient mice

To generate the *Ano5*$^{-/-}$ mouse, the knockout first, conditional ready, lacZ-tagged mutant allele *Ano5*:tm1a(KOMP)Wtsi targeting vector was obtained from the UC Davis KOMP Repository (PG00097_Z_1_G0) (25). This targeting vector was submitted to the Transgenic and Embryonic Stem Cell Core at RINCH for electroporation into ES cells. Clones were screened by PCR using the following primer sets, which produce a 300 bp amplicon from the endogenous *Ano5* locus and a 200 bp amplicon from the *Ano5* cassette insertion locus:

genotyping F 5′-AGTCCTTTTCAGCACAGTCTTTG-3′
genotyping R 5′-TGAGGCAGTGTGGAGTGAGTA-3′

DF38700 5′-GCCAATCATATGGTCTCAGT-3′
LR-loxp R 5′-ACTGATGGCGAGCTCAGACC-3′

Successfully targeted ES cells were then injected into blastocysts of C57BL/6 mice, and embryos transferred to generate chimeras for germline transmission. Transgenic heterozygotes were verified by genotyping and were backcrossed four times to C57BL/6 wild-type, before breeding to homozygosity.

Stocks of *Ano5*$^{-/-}$ and C57BL/6 mice were bred and maintained as homozygous animals in standardized conditions in the Vivarium at the RINCH. They were maintained on Teklad Global Rodent Diet (3.8% Fiber, 18.8% Protein, 5% fat chow) with a 12:12 h dark:light cycle. Procedures used in the experiments were approved by the Institutional Animal Care and Use Committee at Nationwide Children's Hospital (AR12-00004).

Reverse transcriptase–polymerase chain reaction

For both semi-quantitative and quantitative transcript measurements, total RNA was isolated from fresh-frozen muscle shavings using Trizol (Life Technologies, Carslbad, CA), according to the manufacturer's protocol. RNA was then column-purified using the RNAEasy method (Qiagen, Valencia, CA), and quantified by spectrophotometry using a NanoDropLite (Thermo Fisher Scientific, Waltham, MA). cDNA was generated with the High Capactiy cDNA Reverse Transcription Kit (Thermo Fisher Scientific), using equivalent amounts of sample RNA per reaction (200–500 ng), isolated from three individual mice per genotype. For semi-quantitative PCR, equal volumes of cDNA were subjected to 30 PCR cycles, followed by agarose gel electrophoresis. Primers used were: mβAct-rt-5′, CCTGGCCGTCAGGCAGAT; mβAct-rt-3′, GACATGGA GAAGATCTGGCACC; mAno5-rt-F1,CCAACAGAATGAGAACCT; mAno5-rt-R1,GACAGGGGTGGGTACTTTGG; mAno5-rt-F3, CGTT GGCAGCAAGATCAT; mAno5-rt-R3 GGGTACCTATAATCTCTGTA CCTGC. Quantitative PCR was performed and analyzed on a Fast Real-Time PCR System (Thermo Fisher Scientific). Reactions were run with Applied Biosystems primer-FAM probe cocktails for *Ano5* (Mm00624629_m1, Mm01335981_m1), *Ano6* (Mm00614693_m1), *Gapdh* (Mm99999915_g1) and *Hprt* (Mm03024075_m1) in triplicate for each sample. The ΔΔCt method was used to calculate normalized fold-change reductions of *Ano5* and *Ano6* mRNA in *Ano5*$^{-/-}$ muscles when compared with wild-type. *Hprt* and *Gapdh* were each tested with respect to invariance between test groups, and *Hprt* was chosen based upon better stability as a reference gene.

Blue native gel electrophoresis western blotting

Hindlimb muscles were dissected from genotyped *Ano5*$^{+/+}$, *Ano5*$^{+/-}$ and *Ano5*$^{-/-}$ mice and homogenized in 50 mM Bis–Tris, 6N HCl, 50 mM NaCl, 10% w/v glycerol, 0.001% ponceau S, pH 7.2 supplemented with protease inhibitor cocktail III (Calbiochem). Samples were tumbled end over end for 30 min at 4°C and centrifuged at 20 000*g* for 30 min. Soluble protein was collected and protein concentration was measured using the BCA assay. Proteins were separated using blue native polyacrylamide electrophoresis (NativePAGE™ Novex® Bis–Tris Gel System Invitrogen) and transferred to a PVDF membrane. Excess Coomassie Blue dye was washed by agitation over night with PBST. The membrane was blocked for 1 h in 5% non-fat dry milk and stained over night at 4°C with Anti-Ano5 antibody (NeuroMab clone N421A/85) at a 1:100 dilution in PBST + 1% milk. HRP conjugated goat anti-mouse secondary antibody (Biorad) was incubated with membrane for 1 h at room temperature and chemiluminescent signal was measured using ECL and radiographic film. In preliminary experiments, 20 µg protein of each muscle extract was loaded and equal loading was verified by Ponceau-S staining. To facilitate detection of protein in the heterozygote and knockout, the amount of protein loaded in the three lanes was unequal: *Ano5*$^{+/+}$: 6 µg, *Ano5*$^{+/-}$: 10 µg, *Ano5*$^{-/-}$: 16 µg.

Electron microscopy

Segments of TA muscle from 4- to 10-month-old *Ano5*$^{-/-}$ and control mice were removed, stretched to their *in situ* length across a wooden tongue depressor and immersed in 3% glutaraldehyde in 0.1 M phosphate buffer pH 7.0 for 4 h. The muscle was dissected into 2 mm-long tissue blocks, stored in 0.1 M phosphate buffer pH 7.4 overnight, followed by post-fixation in 1% osmium tetroxide for 2 h and dehydration in graded ethanol solutions before plastic embedding. One-micrometer-thick cross-sections were stained with toluidine blue, examined by light microscopy and tissue sections from selected blocks were examined under a Hitachi H-7650 TEM electron microscope utilizing an Advanced Microscopy Techniques camera and software.

Immunofluorescence

Twelve-micrometer-thick cryosections were placed onto Fisher Superfrost microscope slides and blocked with 10% goat serum and 0.1% Tween-20 in PBS for 1 h at room temperature. Slides were incubated in primary antibody for 1 h at room temperature (Anti-FLAG F7425 Sigma-Aldrich, 1:175); Serca1 CaF2-5D2 (Developmental Studies Hybridoma Bank, 1:50). Slides were then rinsed three times with PBS for 1 h at room temperature followed by a 30 min block. Goat-anti-mouse conjugated to Alexa Fluor 594 (A21125, Life Technologies) or goat-anti-rabbit conjugated to Alexa Fluor 568 (A11011, Life Technologies) secondary antibodies were diluted at 1:250 in blocking solution and incubated for 45 min followed by three PBS rinses for 1 h. The sections were mounted with Vectashield (Vector Labs, Burlingame, CA) mounting media and analyzed with a Zeiss Axioskop 2 microscope using a Cy5 filter (excitation, 578–590 nm; emission 603–671 nm) (Zeiss, Thornwood, NY). Image exposure time was standardized using the positive control for each antibody, each day. Images were taken using the Axiovision 4.5 software.

Morphometrics

Fiber diameters

Muscle cross-sectional fiber diameters were determined from TA and gastrocnemius (GAS) muscles from 6-month-old *Ano5*$^{-/-}$ and WT strain control mice ($n = 3$ mice per strain). Muscles were sectioned and stained with hematoxylin and eosin (H&E). Four random 20× images per section per animal were taken with a Zeiss AxioCam MRC5 camera. Fiber diameters were determined by measuring the shortest distance across the muscle fiber using Zeiss Axiovision LE4 software. Fiber diameter histograms were generated from an average of 500–600 fibers per TA and 600–700 fibers per GAS.

Aggregate quantification

Muscle sections from TA and GAS muscles of 10-month-old *Ano5*$^{-/-}$ and WT mice ($n = 3$ mice per tissue and strain) were stained with Gomori Trichrome. Four 20× images were taken and the number of fibers with one or more aggregates were counted using Image J software and expressed as a percentage of the total number of fibers.

Central nuclei quantification

Muscle sections from TA and GAS muscles of 10-month-old *Ano5*$^{-/-}$ and WT mice ($n = 3$ mice per tissue and strain) were

stained with H&E. Four 20× images were taken and the number of fibers with centralized nuclei were counted using Image J software and expressed as a percentage of the total number of fibers.

SDH staining

TA and quadriceps muscles were sectioned at 18 µm and stained with SDH solution consisting of 0.2% nitro blue tetrazolium (NBT) dissolved in 0.1 M succinic acid and 0.1 M phosphate buffer pH 7.4 and incubated at 37°C for 3 h. Following incubation, slides were rinsed with water and dehydrated in serial alcohols then cleared with xylene. Slides were imaged on Zeiss AxioCam MRC5 camera.

rAAV production

The human *ANO5* cDNA was cloned into an AAV2 ITR plasmid using *Not*1 restriction sites between the MHCK7 promoter and polyadenlylation signal. rAAV vectors were produced by a modified cross-packaging approach whereby the AAV type 2 ITRs can be packaged into multiple AAV capsid serotypes (46). Production was accomplished using a standard 3-plasmid DNA $CaPO_4$ precipitation method using HEK293 cells. HEK293 cells were maintained in DMEM supplemented with 10% Cosmic calf serum (CCS, Hyclone). The production plasmids were: (i) pAAV.MHCK7.ANO5, (ii) rep2-cap8 modified AAV helper plasmids encoding cap serotype 8-like isolate rh.74 and (iii) an adenovirus type 5 helper plasmid (pAdhelper) expressing adenovirus E2A, E4 ORF6 and VA I/II RNA genes. Vectors were purified from clarified HEK293 cell lysates by sequential iodixanol gradient purification and anion-exchange column chromatography using a linear NaCl salt gradient as previously described (47). A quantitative PCR-based titration method was used to determine an encapsidated vector genome (vg) titer utilizing a Prism 7500 Taqman detector system (PE Applied Biosystems, Carlsbad, CA) (47).

AAV vector delivery through intramuscular injection to mouse muscle

One- to 2-month-old *Ano5*$^{-/-}$ mice were treated by intramuscular injection of 5×10^{10} vg and 1×10^{11} vg of rAAVrh.74.MHCK7.huANO5.FLAG into TA ($n = 4$) or FDB ($n = 4$) muscles, respectively. For each mouse, the contralateral muscles (right TA and FDB) were used as untreated controls. TA muscles were harvested 4 weeks post-injection and processed for viral potency which included histological and ANO5.FLAG expression. FDB muscle fibers were harvested 10 weeks post-treatment and processed for membrane repair assay.

Membrane repair

Ano5$^{-/-}$ mice were injected with 1×10^{11} vg of AAV.ANO5 into the FDB muscle at 4–5 weeks of age. Muscles were harvested 10 weeks post-injection and subjected to a laser-induced injury. Membrane repair assay was performed on left (treated) and right (untreated) FDB muscles of *Ano5*$^{-/-}$ ($n = 4$) and age-matched C57BL6 ($n = 4$) mice as previously described when the mice were 4 months of age (34). Briefly, FDB fibers were isolated using a solution containing 2% w/v collagenase type I suspended in DMEM. Following dissociation of the muscle, fibers were placed in a glass bottom dish holding 2.5 µM FM1-43 dye in Dulbecco's PBS (no Ca/Mg) supplemented with 1.5 mM Ca^{2+}. Fibers were subjected to laser injury using a FluoView® FV1000 two-photon confocal laser-scanning microscope (Olympus). Fibers were damaged with an 850 nm laser-guided spot of 4.48 µm at 20% power and imaged every 5 s for 190 s to visualize FM1-43 dye uptake. An average of 7–10 fibers were imaged per muscle per mouse, (total 31 WT, 39 *Ano5*$^{-/-}$ and 30 AAV-ANO5 rescued *Ano5*$^{-/-}$ fibers). Fluorescence intensity of dye infiltration surrounding the damage site on the membrane was analyzed with ImageJ software by measuring integrated density of pixel intensity within the defined area. To do so, under a 2× zoom setting on ImageJ, a rectangular box measuring 7.5 µm by 10 µm region of interest is drawn and used to measure the intensity of dye in that region. In the analysis, measured fluorescence intensity at an individual time point was normalized to initial intensity measured at $t = -5$ s (pre-injury) using the equation:

$$\mathrm{NI} = \frac{(I - I_o)}{I_o},$$

where NI is the normalized intensity, I is the measured intensity and I_o is the intensity at $t = -5$ s. When fluorescence intensity was analyzed, values from all fibers from each strain were averaged together. A two-way ANOVA was performed to determine statistical significance between treated and untreated fibers at each time point ($P < 0.001$). *Ano5*$^{-/-}$ fibers, WT fibers and AAV.ANO5 treated *Ano5*$^{-/-}$ fibers were significantly different beginning at 100 s post-injury.

Cardiotoxin injections

Mice were anesthetized with inhaled isoflurane and injected with cardiotoxin (diluted to 10 µM with sterile saline) every 2 weeks, for a total of three rounds. Thirty and 50 µl of cardiotoxin was injected into the left TA and left GAS muscles, respectively, of 8-week-old *Ano5*$^{-/-}$ and aged-matched controls. Sterile saline was injected into contralateral muscle as a sham control. Groups of mice were euthanized and their muscles harvested at 1, 3, 7, 14, 30 and 90 days post final injection of cardiotoxin ($n = 3$ mice per strain per time point). Four 20× images per TA were imaged and fiber diameter was measured on H&E-stained cryosections 1 and 3 months after the final cardiotoxin injection using Axio Vision 4.8. An average of 500–600 muscle fibers per animal was measured.

Behavioral (treadmill) study

7.5 months *Ano5*$^{-/-}$ and aged-matched C57BL6 mice were run once a week until the age of 9.5 months at a –10° decline with a speed of 15 m/min and increased by 1 m every minute until exhaustion was reached ($n = 3$ mice per strain). Each individual test was stopped when the mouse remained on the shock plate (Columbus Instruments) with electrical stimulus set to 20 V for more than 10 s without attempting to engage in exercise. Breaks were defined as the times where the mice ceased running and rested while the treadmill belt returned to the shock plate.

Force generation

Tetanic force measurements were obtained from EDL of 10-month-old mice ($n = 6$ mice per strain), TA from 4-month-old mice ($n = 5$ mice per strain), and diaphragm muscles of 10-month-old *Ano5*$^{-/-}$ and WT mice ($n = 4$ mice per strain). The EDLs were dissected at the tendons and subjected to a physiology protocol to assess function as previously described by our lab and others (48,49) with modifications. During the eccentric contraction protocol, a 5% stretch-re-lengthening procedure executed between 500 and 700 ms (5% stretch over 100 ms, followed by return to optimal length in 100 ms). Following the tetanus and

eccentric contraction protocol, the muscle was removed, wet-weighed, mounted on chuck using gum tragacanth and then frozen in methyl-butane cooled in liquid nitrogen. Force measurements in the TA were performed as previously described (50,51). After the eccentric contractions, the mice were then euthanized and the TA muscle was dissected, weighed and frozen for analysis. For diaphragm force measurements, mice were euthanized and the diaphragm was dissected with rib attachments and central tendon intact, and placed in Krebs–Henselet (K-H) buffer as previously described (52–54). A 2–4 mm wide section of diaphragm was isolated. Diaphragm strips were tied firmly with braided surgical silk (6/0; Surgical Specialties, Reading, PA) at the central tendon, and sutured through a portion of rib bone affixed to the distal end of the strip. Each muscle was transferred to a water bath filled with oxygenated K–H solution that was maintained at 37°C. The muscles were aligned horizontally and tied directly between a fixed pin and a dual-mode force transducer-servomotor (305C; Aurora Scientific, Aurora, Ontario, Canada). Two platinum plate electrodes were positioned in the organ bath so as to flank the length of the muscle. The muscle was stretched to optimal tension of 1 g, and then allowed to rest for 10 min before initiation of the tetanic protocol. Once the muscle was stabilized, the muscle was subjected to a warm-up consisting of three 1 Hz twitches every 30 s followed by three 150 Hz twitches every minute. After a 3 min rest period, the diaphragm was stimulated at 20, 50, 80, 120, 150, 180 Hz, allowing a 2 min rest period between each stimulus, each with a duration of 250 ms to determine maximum tetanic force. Muscle length and weight was measured. The force was normalized for muscle weight and length [CSA: muscle mass (mg)/{Lf(mm) × muscle density (1.06 mg/mm^3)}]. Statistical significance was assessed using an unpaired Student's *t*-test for specific force and two-way ANOVA with repeated measurements for resistance to eccentric contraction protocol.

EMG/EIM

Electrophysiology was performed on 6–8-month *Ano5*$^{-/-}$ and control muscles using methods similar to those previously published (55). Mice were anesthetized using inhaled isoflurane and placed in the prone position with the hindlimbs extended at 45° away from the body of the animal. CMAP amplitudes were measured from bilateral triceps surae muscles following supramaximal sciatic nerve stimulation in mutant ($n = 6$ animals, 12 hindlimbs) and control ($n = 7$ animals, 14 hindlimbs) mice. Needle electromyography was performed in the right GAS muscle to assess for the presence or absence of fibrillation potentials (55). Localized impedance measures, or EIM, was performed in bilateral GAS muscles at frequencies from 1000 Hz to 10 MHz using a Skulpt Inc. EIM1103 system (San Francisco, CA) using methods similar to those previously reported in mouse models of amyotrophic lateral sclerosis and MD (56,57). A fixed electrode array with four 26-gage insulated electromyography needle electrodes (Natus, Middleton, WI) spaced 1 mm apart was used in place of surface electrodes. The electrode array was inserted into the belly of bilateral gastrocnemius muscles in a longitudinal configuration in respect to muscle fiber direction, and two trials of impedance measurements were obtained in each muscle and averaged for a single value in each limb ($n = 6$ animals, 12 hindlimbs for each group). Using the convention from previously published EIM studies and for simplicity, we analyzed reactance, resistance and phase at two current frequencies, 50 and 100 kHz. CMAP amplitudes and impedance characteristics were compared using a two-tailed *t*-test.

Primary muscle cell culture

Primary myoblasts were derived from the hindlimb muscles of 3-month-old *Ano5*$^{-/-}$ mice and age-matched C57BL/6 mice (58,59). Hindlimb muscle was dissected from individual mice and subjected to pronase digestion. The digest was then mechanically dissociated by repeated trituration followed by filtration through a 100 µm vacuum filter (Millipore). Mononucleated cells were resuspended in Ham's F-10 supplemented with 20% fetal bovine serum, 5 ng/ml basic FGF, 100 U/ml penicillin G and 100 µg/ml streptomycin (Growth Media) and were cultured on collagen-coated dishes (Bovine Collagen I Gibco). During the first several passages of the primary cultures, myoblasts were enriched by pre-plating (60).

Primary muscle cell differentiation and fusion index

Cells were differentiated on glass cover slips coated with Entactin-Collagen IV-Laminin (Millipore) at a density of 2×10^5 cells per well in 12-well culture dishes. Myogenic differentiation was induced by culturing the cells in low-glucose DMEM supplemented with 1% Insulin–Selenium–Transferin (Gibco), 100 µg/ml penicillin and 100 µg/ml streptomycin (Differentiation Media) for a period of 3 days. Cells were fixed with 4% paraformaldehyde and stained for MHC (Sigma) to identify differentiated muscle cells and with SYTO 24 Green to visualize nuclei. The fusion index was calculated as the number of nuclei located in cells having more than one nucleus (myotubes) divided by the total number of nuclei. Measurements were done using ImageJ and >1100 nuclei were counted for each experiment. Fusion experiments were done in triplicate with primary isolates from three different mice. Statistical significance was assessed using an unpaired two-tailed Student's *t*-test.

Statistical analysis

Data were expressed as the mean ± SEM and analyzed using unpaired two-tailed *t*-tests using GraphPad Prism 5 (Graphpad Software, La Jolla, CA) unless otherwise specified.

Supplementary Material

Supplementary Material is available at *HMG* online.

Acknowledgements

We thank Nationwide Children's Viral Vector Core for vector production and Nationwide Children's Transgenic and Embryonic Stem Cell Core Lab for Embryonic Stem Cell targeting and blastocyst Injections. The ANO5 targeting vector (Ano5$^{tm1a(KOMP)Wtsi}$-PG00097_Z_1_G01) used for this research project was generated by the trans-NIH KnockOut Mouse Project (KOMP) and obtained from the KOMP Repository (www.komp.org). NIH grants to Velocigene at Regeneron Inc. (U01HG004085) and the CSD Consortium (U01HG004080) funded the generation of gene-targeted ES cells for 8500 genes in the KOMP Program and archived and distributed by the KOMP Repository at UC Davis and CHORI (U42RR024244). For more information or to obtain KOMP products go to www.komp.org or email service@komp.org. The MHCK7 promoter was the kind gift of Dr Steven Hauschka at the University of Washington. We thank the Campus Microscopy and Imaging Facility at the Ohio State University for use of the Multiphoton microscope.

Conflict of Interest statement. None declared.

Funding

This work was supported by National Institutes of Health (1U54HD066409 to L.R.R.-K., EY114852 and AR067786 to H.C.H., 5K12HD001097-17 to W.D.A.); a grant from the Muscular Dystrophy Association to H.C.H.; and Nationwide Children's Hospital Foundation to L.R.R.-K.; and by the National Institutes of Health Training Grant (5T32GM008367-25 to J.M.W.). This work was supported in part by the Emory University Integrated Cellular Imaging Microscopy Core. **IACUC number:** AR12-00004 approved 2/6/12.

References

1. Guiraud, S., Aartsma-Rus, A., Vieira, N.M., Davies, K.E., van Ommen, G.J. and Kunkel, L.M. (2015) The pathogenesis and therapy of muscular dystrophies. *Annu. Rev. Genomics Hum. Genet.*, **16**, 281–308.
2. Constantin, B. (2014) Dystrophin complex functions as a scaffold for signaling proteins. *Biochim. Biophys. Acta*, **1838**, 635–642.
3. Lapidos, K.A., Kakkar, R. and McNally, E.M. (2004) The dystrophin glycoprotein complex: signaling strength and integrity for the sarcolemma. *Circ. Res.*, **94**, 1023–1031.
4. Cooper, S.T. and Head, S.I. (2015) Membrane injury and repair in the muscular dystrophies. *Neuroscientist*, **21**, 653–668.
5. McNeil, P.L. and Baker, M.M. (2001) Cell surface events during resealing visualized by scanning-electron microscopy. *Cell Tissue Res.*, **304**, 141–146.
6. McNeil, P.L. and Kirchhausen, T. (2005) An emergency response team for membrane repair. *Nat. Rev. Mol. Cell Biol.*, **6**, 499–505.
7. Lennon, N.J., Kho, A., Bacskai, B.J., Perlmutter, S.L., Hyman, B. T. and Brown, R.H. Jr (2003) Dysferlin interacts with annexins A1 and A2 and mediates sarcolemmal wound-healing. *J. Biol. Chem.*, **278**, 50466–50473.
8. Glover, L. and Brown, R.H. Jr (2007) Dysferlin in membrane trafficking and patch repair. *Traffic*, **8**, 785–794.
9. Han, R. and Campbell, K.P. (2007) Dysferlin and muscle membrane repair. *Curr. Opin. Cell Biol.*, **19**, 409–416.
10. Bolduc, V., Marlow, G., Boycott, K.M., Saleki, K., Inoue, H., Kroon, J., Itakura, M., Robitaille, Y., Parent, L., Baas, F. *et al.* (2010) Recessive mutations in the putative calcium-activated chloride channel Anoctamin 5 cause proximal LGMD2L and distal MMD3 muscular dystrophies. *Am. J. Hum. Genet.*, **86**, 213–221.
11. Hicks, D., Sarkozy, A., Muelas, N., Koehler, K., Huebner, A., Hudson, G., Chinnery, P.F., Barresi, R., Eagle, M., Polvikoski, T. *et al.* (2011) A founder mutation in Anoctamin 5 is a major cause of limb-girdle muscular dystrophy. *Brain*, **134**, 171–182.
12. Bouquet, F., Cossee, M., Behin, A., Deburgrave, N., Romero, N., Leturcq, F. and Eymard, B. (2012) Miyoshi-like distal myopathy with mutations in anoctamin 5 gene. *Rev. Neurol. (Paris)*, **168**, 135–141.
13. Penttila, S., Palmio, J., Suominen, T., Raheem, O., Evila, A., Muelas Gomez, N., Tasca, G., Waddell, L.B., Clarke, N.F., Barboi, A. *et al.* (2012) Eight new mutations and the expanding phenotype variability in muscular dystrophy caused by ANO5. *Neurology*, **78**, 897–903.
14. Hartzell, H.C., Yu, K., Xiao, Q., Chien, L.T. and Qu, Z. (2009) Anoctamin/TMEM16 family members are Ca^{2+}-activated Cl^- channels. *J. Physiol.*, **587**, 2127–2139.
15. Pedemonte, N. and Galietta, L.J. (2014) Structure and function of TMEM16 proteins (anoctamins). *Physiol. Rev.*, **94**, 419–459.
16. Picollo, A., Malvezzi, M. and Accardi, A. (2015) TMEM16 proteins: unknown structure and confusing functions. *J. Mol. Biol.*, **427**, 94–105.
17. Suzuki, J., Umeda, M., Sims, P.J. and Nagata, S. (2010) Calcium-dependent phospholipid scrambling by TMEM16F. *Nature*, **468**, 834–838.
18. Malvezzi, M., Chalat, M., Janjusevic, R., Picollo, A., Terashima, H., Menon, A.K. and Accardi, A. (2013) Ca^{2+}-dependent phospholipid scrambling by a reconstituted TMEM16 ion channel. *Nat. Commun.*, **4**, 2367.
19. Brunner, J.D., Lim, N.K., Schenck, S., Duerst, A. and Dutzler, R. (2014) X-ray structure of a calcium-activated TMEM16 lipid scramblase. *Nature*, **516**, 207–212.
20. Yu, K., Whitlock, J.M., Lee, K., Ortlund, E.A., Yuan Cui, Y. and Hartzell, H.C. (2015) Identification of a lipid scrambling domain in ANO6/TMEM16F. *Elife*, **4**, e06901.
21. Tran, T.T., Tobiume, K., Hirono, C., Fujimoto, S., Mizuta, K., Kubozono, K., Inoue, H., Itakura, M., Sugita, M. and Kamata, N. (2014) TMEM16E (GDD1) exhibits protein instability and distinct characteristics in chloride channel/pore forming ability. *J. Cell Physiol.*, **229**, 181–190.
22. Suzuki, J., Fujii, T., Imao, T., Ishihara, K., Kuba, H. and Nagata, S. (2013) Calcium-dependent phospholipid scramblase activity of TMEM16 protein family members. *J. Biol. Chem.*, **288**, 13305–13316.
23. Mizuta, K., Tsutsumi, S., Inoue, H., Sakamoto, Y., Miyatake, K., Miyawaki, K., Noji, S., Kamata, N. and Itakura, M. (2007) Molecular characterization of GDD1/TMEM16E, the gene product responsible for autosomal dominant gnathodiaphyseal dysplasia. *Biochem. Biophys. Res. Commun.*, **357**, 126–132.
24. Testa, G., Schaft, J., van der Hoeven, F., Glaser, S., Anastassiadis, K., Zhang, Y., Hermann, T., Stremmel, W. and Stewart, A. F. (2004) A reliable lacZ expression reporter cassette for multipurpose, knockout-first alleles. *Genesis*, **38**, 151–158.
25. Skarnes, W.C., Rosen, B., West, A.P., Koutsourakis, M., Bushell, W., Iyer, V., Mujica, A.O., Thomas, M., Harrow, J., Cox, T. *et al.* (2011) A conditional knockout resource for the genome-wide study of mouse gene function. *Nature*, **474**, 337–342.
26. Gyobu, S., Miyata, H., Ikawa, M., Yamazaki, D., Takeshima, H., Suzuki, J. and Nagata, S. (2015) A role of TMEM16E carrying a scrambling domain in sperm motility. *Mol. Cell Biol.*, **36**, 645–659.
27. Zhao, P., Torcaso, A., Mariano, A., Xu, L., Mohsin, S., Zhao, L. and Han, R. (2014) Anoctamin 6 regulates C2C12 myoblast proliferation. *PLoS One*, **9**, e92749.
28. Liewluck, T., Winder, T.L., Dimberg, E.L., Crum, B.A., Heppelmann, C.J., Wang, Y., Bergen, H.R. III and Milone, M. (2013) ANO5-muscular dystrophy: clinical, pathological and molecular findings. *Eur. J. Neurol.*, **20**, 1383–1389.
29. Milone, M., Liewluck, T., Winder, T.L. and Pianosi, P.T. (2012) Amyloidosis and exercise intolerance in ANO5 muscular dystrophy. *Neuromuscul. Disord.*, **22**, 13–15.
30. Pavlovicova, M., Novotova, M. and Zahradnik, I. (2003) Structure and composition of tubular aggregates of skeletal muscle fibres. *Gen. Physiol. Biophys.*, **22**, 425–440.
31. Agbulut, O., Destombes, J., Thiesson, D. and Butler-Browne, G. (2000) Age-related appearance of tubular aggregates in the skeletal muscle of almost all male inbred mice. *Histochem. Cell Biol.*, **114**, 477–481.
32. Abmayr, S.M. and Pavlath, G.K. (2012) Myoblast fusion: lessons from flies and mice. *Development*, **139**, 641–656.
33. McDade, J.R., Archambeau, A. and Michele, D.E. (2014) Rapid actin-cytoskeleton-dependent recruitment of plasma

membrane-derived dysferlin at wounds is critical for muscle membrane repair. *FASEB J.*, **28**, 3660–3670.
34. Sondergaard, P.C., Griffin, D.A., Pozsgai, E.R., Johnson, R.W., Grose, W.E., Heller, K.N., Shontz, K.M., Montgomery, C.L., Liu, J., Clark, K.R. *et al.* (2015) AAV.Dysferlin overlap vectors restore function in dysferlinopathy animal models. *Ann. Clin. Transl. Neurol.*, **2**, 256–270.
35. Harris, J.B. (2003) Myotoxic phospholipases A2 and the regeneration of skeletal muscles. *Toxicon*, **42**, 933–945.
36. Savarese, M., Di Fruscio, G., Tasca, G., Ruggiero, L., Janssens, S., De Bleecker, J., Delpech, M., Musumeci, O., Toscano, A., Angelini, C. *et al.* (2015) Next generation sequencing on patients with LGMD and nonspecific myopathies: findings associated with ANO5 mutations. *Neuromuscul. Disord.*, **25**, 533–541.
37. Endo, Y., Noguchi, S., Hara, Y., Hayashi, Y.K., Motomura, K., Miyatake, S., Murakami, N., Tanaka, S., Yamashita, S., Kizu, R. *et al.* (2015) Dominant mutations in ORAI1 cause tubular aggregate myopathy with hypocalcemia via constitutive activation of store-operated Ca(2)(+) channels. *Hum. Mol. Genet.*, **24**, 637–648.
38. Bohm, J., Chevessier, F., Maues De Paula, A., Koch, C., Attarian, S., Feger, C., Hantai, D., Laforet, P., Ghorab, K., Vallat, J. M. *et al.* (2013) Constitutive activation of the calcium sensor STIM1 causes tubular-aggregate myopathy. *Am. J. Hum. Genet.*, **92**, 271–278.
39. Krahn, M., Wein, N., Bartoli, M., Lostal, W., Courrier, S., Bourg-Alibert, N., Nguyen, K., Vial, C., Streichenberger, N., Labelle, V. *et al.* (2010) A naturally occurring human minidysferlin protein repairs sarcolemmal lesions in a mouse model of dysferlinopathy. *Sci. Transl. Med.*, **2**, 50ra69.
40. van den Eijnde, S.M., van den Hoff, M.J., Reutelingsperger, C. P., van Heerde, W.L., Henfling, M.E., Vermeij-Keers, C., Schutte, B., Borgers, M. and Ramaekers, F.C. (2001) Transient expression of phosphatidylserine at cell–cell contact areas is required for myotube formation. *J. Cell Sci.*, **114**, 3631–3642.
41. van den Eijnde, S.M., Luijsterburg, A.J., Boshart, L., De Zeeuw, C.I., van Dierendonck, J.H., Reutelingsperger, C.P. and Vermeij-Keers, C. (1997) *In situ* detection of apoptosis during embryogenesis with annexin V: from whole mount to ultrastructure. *Cytometry*, **29**, 313–320.
42. Jeong, J. and Conboy, I.M. (2011) Phosphatidylserine directly and positively regulates fusion of myoblasts into myotubes. *Biochem. Biophys. Res. Commun.*, **414**, 9–13.
43. Hamoud, N., Tran, V., Croteau, L.P., Kania, A. and Cote, J.F. (2014) G-protein coupled receptor BAI3 promotes myoblast fusion in vertebrates. *Proc. Natl Acad. Sci. USA*, **111**, 3745–3750.
44. Hochreiter-Hufford, A.E., Lee, C.S., Kinchen, J.M., Sokolowski, J.D., Arandjelovic, S., Call, J.A., Klibanov, A.L., Yan, Z., Mandell, J.W. and Ravichandran, K.S. (2013) Phosphatidylserine receptor BAI1 and apoptotic cells as new promoters of myoblast fusion. *Nature*, **497**, 263–267.
45. Xu, J., El Refaey, M., Xu, L., Zhao, L., Gao, Y., Floyd, K., Karaze, T., Janssen, P.M. and Han, R. (2015) Genetic disruption of Ano5 in mice does not recapitulate human ANO5-deficient muscular dystrophy. *Skelet. Muscle*, **5**, 43.
46. Rabinowitz, J.E., Rolling, F., Li, C., Conrath, H., Xiao, W., Xiao, X. and Samulski, R.J. (2002) Cross-packaging of a single adeno-associated virus (AAV) type 2 vector genome into multiple AAV serotypes enables transduction with broad specificity. *J. Virol.*, **76**, 791–801.
47. Clark, K.R., Liu, X., McGrath, J.P. and Johnson, P.R. (1999) Highly purified recombinant adeno-associated virus vectors are biologically active and free of detectable helper and wild-type viruses. *Hum. Gene Ther.*, **10**, 1031–1039.
48. Rodino-Klapac, L.R., Janssen, P.M., Montgomery, C.L., Coley, B.D., Chicoine, L.G., Clark, K.R. and Mendell, J.R. (2007) A translational approach for limb vascular delivery of the micro-dystrophin gene without high volume or high pressure for treatment of Duchenne muscular dystrophy. *J. Transl. Med.*, **5**, 45.
49. Liu, M., Yue, Y., Harper, S.Q., Grange, R.W., Chamberlain, J.S. and Duan, D. (2005) Adeno-associated virus-mediated micro-dystrophin expression protects young mdx muscle from contraction-induced injury. *Mol. Ther.*, **11**, 245–256.
50. Hakim, C.H., Grange, R.W. and Duan, D. (2011) The passive mechanical properties of the extensor digitorum longus muscle are compromised in 2- to 20-mo-old mdx mice. *J. Appl. Physiol. (1985)*, **110**, 1656–1663.
51. Wein, N., Vulin, A., Falzarano, M.S., Szigyarto, C.A., Maiti, B., Findlay, A., Heller, K.N., Uhlen, M., Bakthavachalu, B., Messina, S. *et al.* (2014) Translation from a DMD exon 5 IRES results in a functional dystrophin isoform that attenuates dystrophinopathy in humans and mice. *Nat. Med.*, **20**, 992–1000.
52. Beastrom, N., Lu, H., Macke, A., Canan, B.D., Johnson, E.K., Penton, C.M., Kaspar, B.K., Rodino-Klapac, L.R., Zhou, L., Janssen, P.M. *et al.* (2011) mdx((5)cv) mice manifest more severe muscle dysfunction and diaphragm force deficits than do mdx Mice. *Am. J. Pathol.*, **179**, 2464–2474.
53. Rafael-Fortney, J.A., Chimanji, N.S., Schill, K.E., Martin, C.D., Murray, J.D., Ganguly, R., Stangland, J.E., Tran, T., Xu, Y., Canan, B.D. *et al.* (2011) Early treatment with lisinopril and spironolactone preserves cardiac and skeletal muscle in Duchenne muscular dystrophy mice. *Circulation*, **124**, 582–588.
54. Grose, W.E., Clark, K.R., Griffin, D., Malik, V., Shontz, K.M., Montgomery, C.L., Lewis, S., Brown, R.H. Jr, Janssen, P.M., Mendell, J.R. *et al.* (2012) Homologous recombination mediates functional recovery of dysferlin deficiency following AAV5 gene transfer. *PLoS One*, **7**, e39233.
55. Arnold, W.D., Porensky, P.N., McGovern, V.L., Iyer, C.C., Duque, S., Li, X., Meyer, K., Schmelzer, L., Kaspar, B.K., Kolb, S.J. *et al.* (2014) Electrophysiological biomarkers in spinal muscular atrophy: preclinical proof of concept. *Ann. Clin. Transl. Neurol.*, **1**, 34–44.
56. Li, J., Sung, M. and Rutkove, S.B. (2013) Electrophysiologic biomarkers for assessing disease progression and the effect of riluzole in SOD1 G93A ALS mice. *PLoS One*, **8**, e65976.
57. Li, J., Geisbush, T.R., Rosen, G.D., Lachey, J., Mulivor, A. and Rutkove, S.B. (2014) Electrical impedance myography for the *in vivo* and *ex vivo* assessment of muscular dystrophy (mdx) mouse muscle. *Muscle Nerve*, **49**, 829–835.
58. Bondesen, B.A., Mills, S.T., Kegley, K.M. and Pavlath, G.K. (2004) The COX-2 pathway is essential during early stages of skeletal muscle regeneration. *Am. J. Physiol. Cell Physiol.*, **287**, C475–C483.
59. Mitchell, P.O. and Pavlath, G.K. (2001) A muscle precursor cell-dependent pathway contributes to muscle growth after atrophy. *Am. J. Physiol. Cell. Physiol.*, **281**, C1706–C1715.
60. Rando, T.A. and Blau, H.M. (1994) Primary mouse myoblast purification, characterization, and transplantation for cell-mediated gene therapy. *J. Cell Biol.*, **125**, 1275–1287.